Editors' Suggestion

Third-Order Nonlinear Hall Effect in Altermagnet RuO_2

R. Y. Chu,[1,*] L. Han,[1,*] Z. H. Gong,[2,*] X. Z. Fu,[3] H. Bai,[1] S. X. Liang,[1] C. Chen,[1] S-W. Cheong,[4] Y. Y. Zhang,[3] J. W. Liu,[3] Y. Y. Wang,[1] F. Pan,[1] H. Z. Lu,[2,5,†] and C. Song[1,‡]

[1]*Key Laboratory of Advanced Materials (MOE), School of Materials Science and Engineering, Tsinghua University, Beijing 100084, China*

[2]*State Key Laboratory of Quantum Functional Materials, Department of Physics, and Guangdong Basic Research Center of Excellence for Quantum Science, Southern University of Science and Technology (SUSTech), Shenzhen 518055, China*

[3]*Department of Physics, The Hong Kong University of Science and Technology, Hong Kong 999077, China*

[4]*Rutgers Center for Emergent Materials and Department of Physics and Astronomy, Rutgers University, Piscataway, New Jersey 08854, USA*

[5]*Quantum Science Center of Guangdong-Hong Kong-Macao Greater Bay Area (Guangdong), Shenzhen 518045, China*

(Received 4 June 2025; accepted 15 October 2025; published 17 November 2025)

Altermagnets are a novel class of magnetic materials with cutting-edge advantages. Identifying altermagnets, i.e., exploring their distinguishing fingerprints, is vital but challenging. The as-reported spontaneous anomalous Hall effect is not universally present in all altermagnets due to magnetic symmetry constraints, and the second-order nonlinear Hall effect is prohibited by spatial-inversion symmetry. Here, we report the experimental discovery of a third-order nonlinear Hall effect (TNHE) in RuO_2 thin films. TNHE emerges when current is applied along [110] or $[\bar{1}10]$ crystal direction for $RuO_2(001)$, as the second-order currents induce a magnetization by breaking orthogonal mirror and rotation symmetries of this altermagnet. These symmetry-breaking conditions also enforce a twofold angular dependence of TNHE concerning current direction in the $RuO_2(001)$ plane. Moreover, temperature-dependent measurements and scaling law analysis reveal that TNHE is governed primarily by the third-order skew scattering mechanism. Our findings establish TNHE as a transport fingerprint of altermagnet RuO_2, which can be generalized to other altermagnets such as d-wave V_2X_2O (X = Se or Te) and g-wave MnTe and CrSb.

DOI: 10.1103/rv1n-vr4p

Altermagnets are characterized by nonrelativistic alternating spin splitting in momentum space and collinear compensated magnetic moments in real space, representing a novel class of magnetic material beyond traditional ferromagnets and antiferromagnets [1–3]. They exhibit exotic time-reversal (T) symmetry-breaking phenomena, including spin-splitting torques (SSTs) [4–7], tunneling magnetoresistance [8,9], the anomalous Hall effect (AHE) [10–14], and the anomalous Nernst effect [15,16]. Meanwhile, altermagnets retain robustness against external magnetic perturbations, lack stray fields, and support ultrafast Néel vector dynamics in the terahertz range [17,18]. These unique properties make them promising candidates in spintronic applications. A central and ongoing challenge, however, lies in establishing reliable fingerprints for altermagnets, which are crucial for both their fundamental understanding and technological exploitation. Recently, angle-resolved photoemission spectroscopy (ARPES) [19–21] and SSTs provide compelling evidence of spin-splitting band structures in altermagnets, offering valuable insights from spectroscopic and transport perspectives. However, ARPES is inherently constrained by surface states and weak spin polarization, while SSTs are complicated by anisotropic conductivity and are largely restricted to d-wave altermagnets. These limitations underscore the need to identify alternative, simpler, and more robust fingerprints for altermagnets.

The AHE is a hallmark T-symmetry-breaking magneto-electronic transport phenomenon, extensively observed in ferromagnets and noncollinear antiferromagnets [10,11]. In altermagnets, although T symmetry is broken, AHE either vanishes or becomes negligibly small due to stringent magnetic symmetry constraints. Experimentally, the AHE is induced by lowering the symmetry in CrSb [14] or by manipulating the Néel vector orientation in RuO_2 under a strong magnetic field [22]. However, the AHE cannot be regarded as a definitive fingerprint for altermagnets because it lacks both universality and spontaneity in altermagnets. Notably, recent progress has demonstrated the second-order nonlinear Hall effect (SNHE) as a probe of the Néel vector in fully compensated antiferromagnets. The SNHE arises from quantum geometry, including the Berry curvature dipole and

*These authors contributed equally to this work.
†Contact author: luhz@sustech.edu.cn
‡Contact author: songcheng@mail.tsinghua.edu.cn

quantum metric dipole [23,24]. However, this response is limited to materials with broken space inversion (P) symmetry. Consequently, neither the AHE nor SNHE can serve as fingerprints for altermagnets. Intriguingly, theoretical studies predicted that even-order currents can induce magnetization in altermagnets, leading to a high odd-order nonlinear Hall effect (HNHE). Despite these compelling predictions [25–28], experimental verification of HNHE remains elusive to date.

In widely studied altermagnets such as MnTe, and Mn_5Si_3, the presence of spontaneous AHE obscures possible signals of HNHE. In contrast, RuO_2, with its collinearly compensated Néel vector and well-defined symmetry, provides an ideal platform for investigating HNHE. RuO_2 is a prototypical d-wave altermagnet, with its magnetism and altermagnetism revealed by neutron diffraction [29], x-ray scattering [30], ARPES [31], and spin-dependent transport studies [4–7,32–36]. Nonetheless, certain experiments report the absence of long-range magnetic order and band splitting in RuO_2 [37,38]. More recent investigations, however, demonstrate the magnetic order in RuO_2 thin films using ARPES [31,39], optical second-harmonic generation [40], optically induced spin polarization [41], and tunneling magnetoresistance [42]. Importantly, thin film size effects may account for the ongoing controversy surrounding the magnetism of RuO_2. Probing HNHE in RuO_2 thin films would not only establish transport-based evidence of altermagnetism but also provide a fingerprint signature applicable to a broader class of altermagnets.

We first analyze the symmetry prerequisites for observing HNHE. The magnetic point group of RuO_2 is $4'/mmm'$, which hosts fourfold rotational symmetry combined with T symmetry along the [001] axis [29,30]. The crystal possesses mirror planes ($M_{[100]}$, $M_{[010]}$, and $M_{[001]}$), twofold rotation axes ($C_{2[100]}$, $C_{2[010]}$, and $C_{2[001]}$) [Fig. 1(a)], and magnetic mirror symmetries ($M_{[110]} \times T$, $M_{[\bar{1}10]} \times T$) [Fig. 1(b)]. For simplicity, the local oxygen atom structures around Ru spins, which exhibit twofold symmetry, can be treated as directors [schematically shown as green ellipsoids in Fig. 1(c)]. HNHE emerges only when the symmetry set $\{P \times T, T, M_x, M_y, C_{2x}, C_{2y}, M_z \times T, C_{2z} \times T\}$ is simultaneously broken. In this case, a longitudinal current along the x or y axis can generate a transverse high odd-order Hall voltage along the orthogonal direction. Here, $P \times T$ denotes the combined P and T, $M_\alpha[\alpha = x, y, z]$ refers to mirror symmetry perpendicular to the α axis, and $C_{2\alpha}$ denotes a twofold rotation around the α axis. These symmetries can be broken by external perturbations such as strain, electric field (current), or magnetic field. RuO_2 intrinsically breaks $\{T, P \times T\}$. The film normal is defined as the z axis. Furthermore, $M_z \times T$, and $C_{2z} \times T$ are guaranteed broken when the z axis is not aligned along [110] or $[\bar{1}10]$. Consequently, $RuO_2(110)$ is not expected to exhibit HNHE.

The simplest film configurations for realizing HNHE are $RuO_2(001)$ and $RuO_2(100)$, both of which naturally break $M_z \times T$ and $C_{2z} \times T$ symmetries. The current breaks the mirror symmetry when its direction is not parallel to the mirror plane. Since current is a polar vector, a component perpendicular to a mirror plane reverses direction under the mirror operation, thereby breaking that symmetry. For $RuO_2(001)$ film, $M_{[001]}$ mirror is preserved, which means that $M_{[001]} \times T$ is broken. Figure 1(c) illustrates the mirror planes ($M_{[100]}$ and $M_{[010]}$, purple lines), and twofold rotation axes ($C_{2[100]}$ and $C_{2[010]}$, bright blue arrows) in $RuO_2(001)$ film. To generated HNHE, $M_{[100]}$, $M_{[010]}$, $C_{2[100]}$, $C_{2[010]}$ need to be broken simultaneously. This condition is satisfied when current is applied along the [110] or $[\bar{1}10]$ directions, where the even-order currents induce magnetization, leading to HNHE.

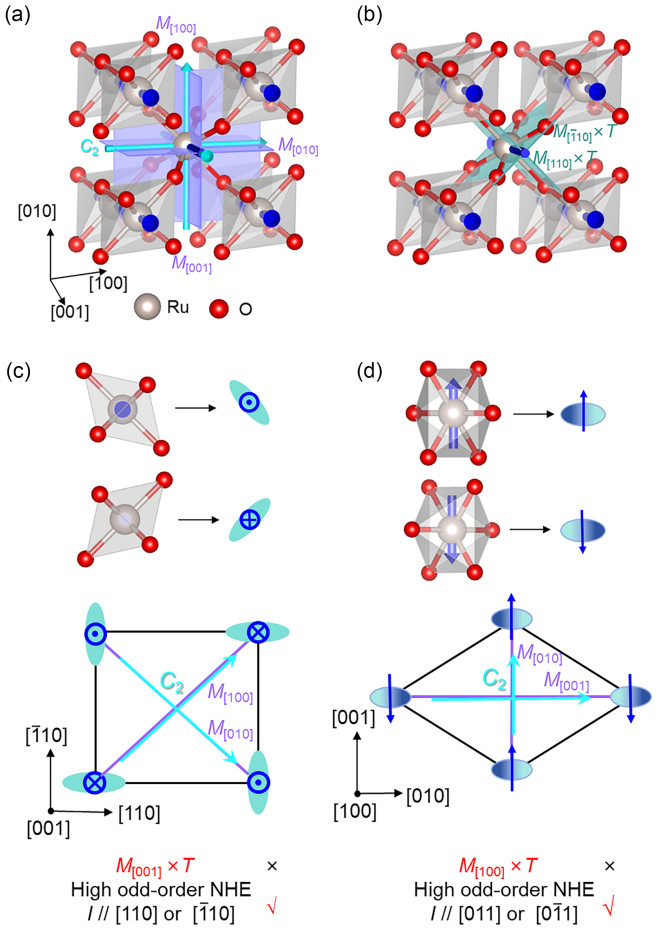

FIG. 1. Symmetry analysis of HNHE in RuO_2. (a),(b) Crystal and magnetic structure of the rutile RuO_2 with (a) mirror planes ($M_{[100]}$, $M_{[010]}$, and $M_{[001]}$), twofold rotation axes ($C_{2[100]}$, $C_{2[010]}$, and $C_{2[001]}$), and (b) magnetic mirror symmetry ($M_{[110]} \times T$, $M_{[\bar{1}10]} \times T$). Gray and red spheres represent Ru and O atoms, respectively. Bright blue arrows indicate Ru local moments. (c) Symmetry elements of $RuO_2(001)$ film, including mirror planes ($M_{[100]}$, $M_{[010]}$) and twofold rotation axis ($C_{2[100]}$, $C_{2[010]}$). (d) Symmetry elements of $RuO_2(100)$ film, including mirror planes ($M_{[010]}$, $M_{[001]}$) and twofold rotation axis ($C_{2[010]}$, $C_{2[001]}$). The local nonmagnetic atomic structure around the spins can be treated as directors (green ellipsoids). Dots and crosses denote Ru local magnetic moments pointing out of or into the plane, respectively.

In contrast, when the current flows along [100] or [010], either $M_{[010]}$ or $M_{[100]}$ remains preserved, suppressing the response. Thus, the maximum HNHE is expected for current along [110] or $[\bar{1}10]$, and vanishes for [100] or [010]. For $RuO_2(100)$ film, $M_{[100]}$ is preserved, so $M_{[100]} \times T$ is broken. In this case, $M_{[010]}$, $M_{[001]}$, $C_{2[010]}$, and $C_{2[001]}$ are broken simultaneously when current is applied along [011] or $[0\bar{1}1]$ direction [Fig. 1(d)].

To experimentally probe HNHE, we deposited 5 nm thick RuO_2 films with (001) and (100) orientations on TiO_2 substrates using magnetron sputtering. The high crystalline quality and single-phase nature were confirmed through x-ray diffraction [43]. The samples were subsequently patterned into Hall bar devices [Fig. 2(a)]. An ac current (I) with a fixed frequency of 166 Hz was applied along the device channel, and both longitudinal and transverse voltage drops were recorded at the fundamental and third-harmonic frequencies. Control measurements across a frequency range of 26–166 Hz confirmed that the results were frequency independent, excluding possible artifacts such as spurious capacitive coupling. The first-harmonic longitudinal voltage ($V_{\parallel}^{1\omega}$) and transverse voltage ($V_{\perp}^{1\omega}$) scale linearly with the applied current. Notably, $V_{\perp}^{1\omega}$ is about 3% of $V_{\parallel}^{1\omega}$ [Fig. 2(b)], which we attribute to a small misalignment between the electrodes and the sample strip.

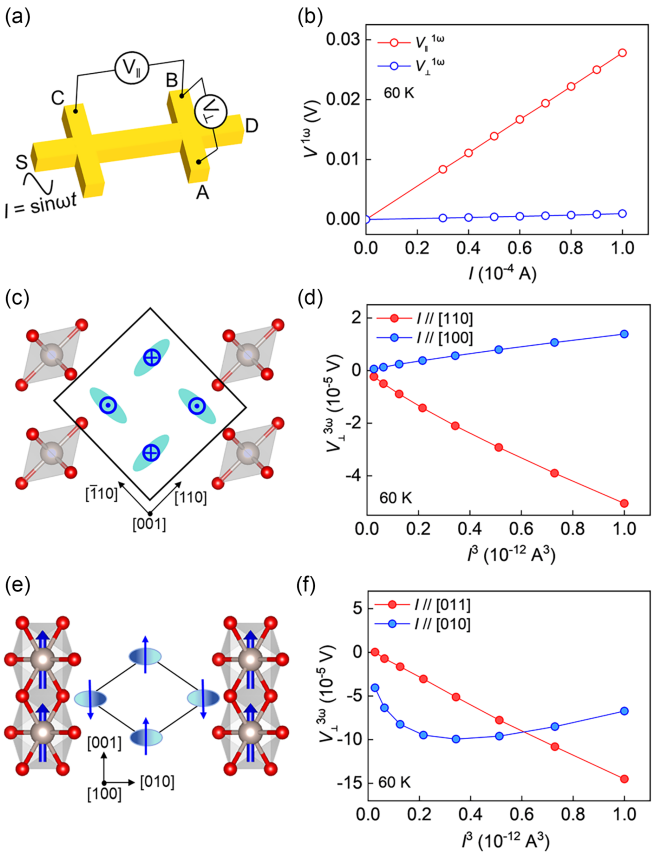

FIG. 2. TNHE in RuO_2. (a) Schematic diagram of a Hall bar device. An ac current is applied between S and D, while transverse (A−B) and longitudinal (C−B) voltages are recorded. (b) $V_{\parallel}^{1\omega}$ and $V_{\perp}^{1\omega}$ as a function of I. (c),(e) Crystal orientation and schematic representation with directors for (c) $RuO_2(001)$ film and (e) $RuO_2(100)$ film. (d),(f) $V_{\perp}^{3\omega}$ as a function of I^3 for (d) $RuO_2(001)$ film and (f) $RuO_2(100)$ film.

The third-order nonlinear Hall effect (TNHE), corresponding to the lowest-order manifestation of HNHE, is investigated within the framework of crystal symmetry. In $RuO_2(001)$ films [Fig. 2(c)], when current is applied along [110] direction, the third-harmonic transverse voltage ($V_{\perp}^{3\omega}$) exhibits a cubic dependence on current amplitude. For $I = 100$ μA, $V_{\perp}^{3\omega}$ reaches -4.0×10^{-5} V [Fig. 2(d)]. By contrast, when current is applied along the [100] directions, $V_{\perp}^{3\omega}$ is significantly smaller, with a positive value of $+1.0 \times 10^{-5}$ V. The sign of $V_{\perp}^{3\omega}$ reverses upon switching either the current direction or the Hall probe polarity [43]. To clarify the origin of this unexpected $V_{\perp}^{3\omega}$ for $I//[100]$, we perform analogous measurements on paramagnetic $IrO_2(001)$, which shares the same rutile crystal structures as RuO_2. Remarkably, IrO_2 exhibits a comparable signal of $+1.0 \times 10^{-5}$ V [43], indicating that this component arises intrinsically from the rutile lattice rather than magnetic ordering. The dependence of both magnitude and sign of $V_{\perp}^{3\omega}$ on the crystal orientation highlights the strong crystallographic sensitivity of TNHE.

For $RuO_2(100)$ films [Fig. 2(e)], a pronounced $V_{\perp}^{3\omega}$ of approximately -1.5×10^{-4} V is observed when current flows along the [011] direction. By contrast, no cubic dependence is detected when current is applied along [010] direction [Fig. 2(f)]. For $RuO_2(110)$ film, no TNHE is detected, in agreement with predictions based on symmetry analysis [43]. These results are fully consistent with symmetry-based predictions for RuO_2 film, underscoring the decisive role of crystalline symmetry in nonlinear transport. In general, TNHE in RuO_2 thin films emerges only when the full set of symmetries $\{P \times T, T, M_x, M_y, C_{2x}, C_{2y}, M_z \times T, C_{2z} \times T\}$ is simultaneously broken. We further investigated the size dependence of the TNHE in $RuO_2(100)$ Hall bars. For widths exceeding 30 μm, the effective region no longer maintains preferential domain alignment, leading to complete cancellation of the TNHE contributions from oppositely oriented domains. Crucially, all of the measurements were performed in the absence of an external magnetic field. This contrasts with a recent report of Berry curvature quadrupole (BCQ) induced TNHE in the A-type kagome antiferromagnet FeSn [49], which required an 8 T magnetic field to align spins and lower the symmetry. Our findings thus demonstrate spontaneous TNHE in RuO_2, arising solely from intrinsic crystal symmetry.

To investigate the crystallographic dependence of TNHE more precisely, $RuO_2(001)$ and $IrO_2(001)$ films are fabricated into circular disc device [Fig. 3(a)] [44,50]. Each device

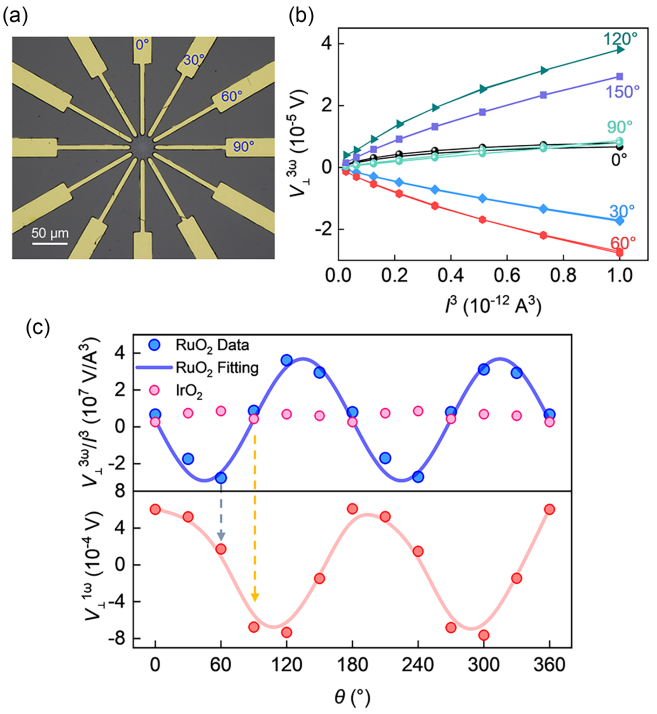

FIG. 3. Angular dependence of TNHE. (a) Optical image of a circular disk device. The current is injected through two of the 12 electrodes, and the Hall voltage drop across the electrodes perpendicular to where the current is probed. (b) $V_\perp^{3\omega}$ depends linearly on I^3 for different current directions. (c) $V_\perp^{3\omega}/I^3$ (upper panel) in $RuO_2(001)$ and $IrO_2(001)$ films and $V_\perp^{1\omega}$ (lower panel) in $RuO_2(001)$ film as a function of θ.θ is the angle between the current and the [010] direction, measured in a clockwise rotating frame. All measurements were conducted at 60 K.

features 12 symmetrically arranged electrodes, allowing current injection through a selected electrode pair while measuring the perpendicular voltages $V_\perp^{1\omega}$ and $V_\perp^{3\omega}$. In $RuO_2(001)$ film, $V_\perp^{3\omega}$ exhibits a cubic dependence on current across all channels [Fig. 3(b)]. The slope of $V_\perp^{3\omega}$ versus I^3 ($V_\perp^{3\omega}/I^3$) as a function of angle θ is summarized in Fig. 3(c) (top panel), showing a pronounced twofold symmetry well described by a $\sin 2\theta$ dependence (blue curve), where θ denotes the angle between current and the [010] direction. $V_\perp^{3\omega}/I^3$ reaches its extrema when the current is aligned along [110] or [$\bar{1}$10], where both $M_{[100]}$ and $M_{[010]}$ are simultaneously broken. Conversely, $V_\perp^{3\omega}$ nearly vanishes when the current is along [100] or [010], where a mirror plane parallel to the current remains preserved. In contrast, in $IrO_2(001)$ film, $V_\perp^{3\omega}/I^3$ exhibits no angular dependence, indicating that the third-order Hall voltage arises solely from the intrinsic rutile crystal structures. This comparison confirms that the pronounced angular dependence of $V_\perp^{3\omega}$ in $RuO_2(001)$ originates from its intrinsic magnetic order. This angular dependence in $RuO_2(001)$ is consistently reproduced in a circular disk device with 16 electrode contacts [43], confirming the robustness and reproducibility of the symmetry-governed TNHE.

$V_\perp^{1\omega}$ exhibits a linear dependence on current, and its angular dependence is summarized in Fig. 3(c) (bottom panel). As indicated by the gray arrow, $V_\perp^{3\omega}/I^3$ reaches its extrema precisely where $V_\perp^{1\omega}$ approaches zero. Conversely, as indicated by the orange arrow, $V_\perp^{3\omega}/I^3$ vanishes when $V_\perp^{1\omega}$ is maximized. This complementary behavior demonstrates that the third-harmonic response is not an artifact of the first-harmonic transverse voltage, as the two signals display distinct angular dependencies. Furthermore, contributions from the longitudinal voltage $V_\parallel$ can be excluded. Under $C_{4z}T$ symmetry, the longitudinal resistance remains isotropic, ensuring that $V_\perp^{3\omega}$ cannot originate from $V_\parallel$ [43].

The angular dependence of TNHE response can be quantitatively described by the following analytical expression, derived from the $4'/mmm'$ magnetic point group symmetry [43]:

$$j_H^{(3)} = E_0^3\left[\chi_{xyyy}\sin 2\theta - \frac{1}{4}(3\chi_{xxyy} - \chi_{xxxx})\sin 4\theta\right]. \quad (1)$$

Here, χ_{abcd} represents the components of the third-order susceptibility tensor. The χ_{abcd} terms that are T-odd exhibit a twofold angular dependence, whereas T-even terms produce a fourfold angular dependence. The observed twofold angular dependence confirms that TNHE originates from the T-odd component χ_{xyyy}. Consequently, $V_\perp^{3\omega}$ reverse sign when the magnetic order parameter is inverted under T operation. In conventional magnets, such reversal is typically achieved by applying an external magnetic field. In contrast, the intrinsic crystalline anisotropy of altermagnets enables a more direct approach—switching the magnetic order via a 90° crystal rotation [28]. This effect is demonstrated in Fig. 3(c) (top panel), where $V_\perp^{3\omega}$ changes sign upon a 90° rotation. These results provide compelling evidence of magnetic ordering in RuO_2. Moreover, the negligible second-harmonic transverse voltage is consistent with the preserved P symmetry of RuO_2, with the small residual signal likely arising from thermal effects [43,45].

To explore the possible microscopic mechanisms underlying TNHE in RuO_2, we derive the scaling law [46,47], i.e., the relation between the third-order Hall conductance χ_{yxxx} and linear longitudinal conductivity σ_{xx},

$$\chi_{yxxx} = C_6\sigma_{xx}^6 + C_5\sigma_{xx}^5 + C_4\sigma_{xx}^4 + C_3\sigma_{xx}^3 + C_2\sigma_{xx}^2 + C_1\sigma_{xx} + C_0, \quad (2)$$

where the seven fitting parameters C_i carry the information of microscopic mechanisms, as categorized in Table I. From the experimental data, χ_{yxxx} can be determined as

$$\chi_{yxxx} = \frac{V_\perp^{3\omega}\sigma_{xx}}{(V_\parallel^{1\omega})^3}\frac{L^3}{W}, \quad (3)$$

where L and W is the length and cross-sectional area of the Hall bar, respectively. The temperature dependence of the longitudinal conductivity σ_{xx} is shown in Fig. 4(a), where

TABLE I. Dependence of the parameters C_i in the scaling law Eq. (2) on the 13 microscopic mechanisms under the symmetry of RuO_2, including the side jump (SJ), skew scattering (SK), mixed side jump and second-order skew scattering (S2SK), mixed second-order side jump and skew scattering (2SSK), third-order side jump (3SJ), third-order skew scattering (3SK), BCQ, mixed Berry curvature, side jump, and skew scattering (BSSK), Berry curvature and second-order side jump (B2SJ), Berry curvature and second-order skew scattering (B2SK), quantum metric and side jump (QSJ), quantum metric and skew scattering (QSK), and third-order intrinsic (TOI) mechanisms.

Parameters	Mechanisms
$C_6(\mathrm{V}^{-2}\cdot\mathrm{S}^{-5}\cdot\mathrm{m}^2)$	3SK
$C_5(\mathrm{V}^{-2}\cdot\mathrm{S}^{-4}\cdot\mathrm{m}^2)$	3SK, S2SK
$C_4(\mathrm{V}^{-2}\cdot\mathrm{S}^{-3}\cdot\mathrm{m}^2)$	3SK, S2SK, B2SK, 2SSK, SK
$C_3(\mathrm{V}^{-2}\cdot\mathrm{S}^{-2}\cdot\mathrm{m}^2)$	3SK, S2SK, B2SK, BSSK, 2SSK, 3SJ, SK, SJ
$C_2(\mathrm{V}^{-2}\cdot\mathrm{S}^{-1}\cdot\mathrm{m}^2)$	3SK, S2SK, B2SK, BSSK, B2SJ, 2SSK, QSJ, QSK, 3SJ, SK, SJ, BCQ
$C_1(\mathrm{V}^{-2}\cdot\mathrm{m}^2)$	3SK, S2SK, B2SK, BSSK, B2SJ, 2SSK, QSJ, QSK, 3SJ
$C_0(\mathrm{V}^{-2}\cdot\mathrm{S}\cdot\mathrm{m}^2)$	3SK, S2SK, B2SK, BSSK, B2SJ, 2SSK, QSJ, QSK, 3SJ, TOI

σ_{xx} decreases from 7.37×10^6 to 7.00×10^6 S/m as the temperature increases from 35 to 100 K, indicating metallic behavior. $V_\perp^{3\omega}$ scales linearly with I^3 at all measured temperatures [Fig. 4(b)]. The same Hall bar device from Fig. 2 [with $I//[110]$ in $RuO_2(001)$ film] is used for these measurements. For this range of temperature, χ_{yxxx} as a function of σ_{xx} is summarized in Fig. 4(c).

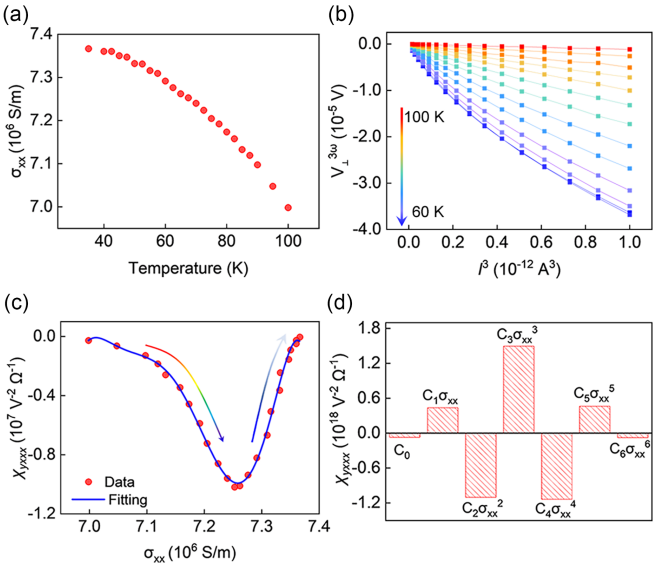

FIG. 4. Scaling law between χ_{yxxx} and σ_{xx}. (a) Temperature dependence of σ_{xx} for the same Hall bar device as in Fig. 2. (b) $V_\perp^{3\omega}$ depends linearly on I^3 at temperatures ranging from 60 to 100 K. (c) Measured χ_{yxxx} as a function of σ_{xx} at temperatures ranging from 35 to 100 K (red dots). The blue line represents the fit to the data using Eq. (2). (d) Weights of the seven $C_i\sigma_{xx}^i$ terms in Eq. (3) at $\sigma_{xx}=7.26\times10^6$ S/m. The length and cross-sectional area of the Hall bar are 20 μm and 0.01 μm^2, respectively.

With the help of the scaling law in Eq. (2), we fit the relation between χ_{yxxx} and σ_{xx} in Fig. 4(c). The fitting can give the weights of the seven $C_i\sigma_{xx}^i$ terms in the scaling law [Fig. 4(d)]. The finite $C_6\sigma_{xx}^6$ term in Fig. 4(d) directly points to the contribution of the third-order skew scattering (3SK) mechanism, since, according to Table I, 3SK is the only contribution to this term. The 3SK mechanism corresponds to asymmetric scattering of spin-up and spin-down electrons through three successive events. Furthermore, Table I indicates that 3SK contributes to all seven $C_i\sigma_{xx}^i$ terms, albeit with different relative weights [43]. The experimentally extracted weights in Fig. 4(d) follow the ratio $C_6\sigma_{xx}^6:C_5\sigma_{xx}^5:C_4\sigma_{xx}^4:C_3\sigma_{xx}^3:C_2\sigma_{xx}^2:C_1\sigma_{xx}:C_0 = -1.09:6.45:-15.9:20.9:-15.4:6.09:-1$, which is in close correspondence with the theoretical coefficients of $C_{111111}^{3\mathrm{SK}}$ [43],

$$1:-6:15:-20:15:-6:1,$$

where each "1" in the subscript "111111" denotes a correlation between two dynamical scattering events (e.g., phonon-mediated). This consistency in the weights between experiment and scaling law theory [47] provides compelling evidence that the dominant microscopic mechanism of TNHE in altermagnetic RuO_2 is the third-order skew scattering. Notably, in thicker 30 nm RuO_2 films, the observed $V_\perp^{3\omega}$ arises instead from coupling between transverse resistance and Joule heating, rather than from 3SK, underscoring the critical role of film thickness in probing TNHE [43].

Recent theoretical study reports a novel quantum geometry—BCQ—as a key contributor to TNHE in d-wave altermagnets [28]. In contrast, by systematically considering all 13 relevant microscopic mechanisms, our experimental results demonstrate that TNHE in RuO_2 is predominantly governed by 3rd skew scattering. This contrast underscores the rich diversity of microscopic mechanisms that can drive the TNHE in altermagnets. Notably, TNHE in RuO_2 significantly exceeds the third-order responses associated with Berry connection polarizability or BCQ, such as T_dMoTe$_2$ and FeSn [44,49,51]. These findings establish RuO_2 as a highly promising platform for efficient rectification based on nonlinear transport. HNHE, as a fingerprint transport feature of altermagnets, is generally applicable to d-wave V_2X_2O (X = Se or Te) [52,53] as well as g-wave altermagnets such as MnTe and CrSb [43,48].

In summary, we report the discovery of the TNHE in RuO_2 thin films, establishing it as a characteristic fingerprint of altermagnets that arises when the symmetries $\{P\times T, T, M_x, M_y, C_{2x}, C_{2y}, M_z\times T, C_{2z}\times T\}$ are broken. For $RuO_2(001)$, TNHE emerges when the current is applied along the [110] or $[\bar{1}10]$ direction, where the symmetries $\{M_{[100]}, M_{[010]}, C_{2[100]}, C_{2[010]}, M_{[001]}\times T, C_{2[001]}\times T\}$ are broken. For $RuO_2(100)$, TNHE appears when the

current is along the [011] or $[0\bar{1}1]$ direction; $\{M_{[010]}, M_{[001]}, C_{2[010]}, C_{2[001]}, M_{[100]} \times T, C_{2[100]} \times T\}$ are broken in this case. A pronounced twofold angular dependence of TNHE in $RuO_2(001)$ plane further confirms the underlying magnetic order. Temperature-dependent measurements and scaling analysis identify third-order skew scattering as the dominant microscopic mechanism. Altogether, these findings demonstrate that TNHE provides both a nonlinear transport fingerprint of altermagnets and direct evidence for the magnetic order in RuO_2 thin films.

Acknowledgments—This work was supported by the National Key R&D Program of China (Grants No. 2022YFA1402603 and No. 2022YFA1403700), Tsinghua University Initiative Scientific Research Program, National Natural Science Foundation of China (Grants No. 52225106, No. 12241404, No. T2394471, No. 12525401, and No. 12350402), Natural Science Foundation of Beijing Municipality (Grant No. F251037), China Postdoctoral Science Foundation (Grant No. 2025M773328), Hong Kong Research Grants Council (Grants No. 16303821, No. 16306722, and No. 16304523), Guangdong Basic and Applied Basic Research Foundation (No. 2023B0303000011), and the New Cornerstone Science Foundation through the XPLORER PRIZE.

Data availability—The data that support the findings of this article are openly available [54].

[1] L. Šmejkal, J. Sinova, and T. Jungwirth, Beyond conventional ferromagnetism and antiferromagnetism: a phase with nonrelativistic spin and crystal rotation symmetry, Phys. Rev. X **12**, 031042 (2022).
[2] L. Šmejkal, J. Sinova, and T. Jungwirth, Emerging research landscape of altermagnetism, Phys. Rev. X **12**, 040501 (2022).
[3] C. Song, H. Bai, Z. Y. Zhou, L. Han, H. Reichlova, J. H. Dil, J. W. Liu, X. Z. Chen, and F. Pan, Altermagnets as a new class of functional materials, Nat. Rev. Mater. **10**, 473 (2025).
[4] R. González-Hernández, L. Šmejkal, K. Výborný, Y. Yahagi, J. Sinova, T. Jungwirth, and J. Železný, Efficient electrical spin splitter based on nonrelativistic collinear antiferromagnetism, Phys. Rev. Lett. **126**, 127701 (2021).
[5] H. Bai, L. Han, X. Y. Feng, Y. J. Zhou, R. X. Su, Q. Wang, L. Y. Liao, W. X. Zhu, X. Z. Chen, F. Pan, X. L. Fan, and C. Song, Observation of spin splitting torque in a collinear antiferromagnet RuO_2, Phys. Rev. Lett. **128**, 197202 (2022).
[6] S. Karube, T. Tanaka, D. Sugawara, N. Kadoguchi, M. Kohda, and J. Nitta, Observation of spin-splitter torque in collinear antiferromagnetic RuO_2, Phys. Rev. Lett. **129**, 137201 (2022).
[7] A. Bose, N. J. Schreiber, R. Jain, D.-F. Shao, H. P. Nair, J. Sun, X. S. Zhang, D. A. Muller, E. Y. Tsymbal, D. G. Schlom, and D. C. Ralph, Tilted spin current generated by the collinear antiferromagnet ruthenium dioxide, Natl. Electron. Rev. **5**, 267 (2022).
[8] D.-F. Shao, S.-H. Zhang, M. Li, C.-B. Eom, and E. Y. Tsymbal, Spin-neutral currents for spintronics, Nat. Commun. **12**, 7061 (2021).
[9] L. Šmejkal, A. B. Hellenes, R. González-Hernández, J. Sinova, and T. Jungwirth, Giant and tunneling magnetoresistance in unconventional collinear antiferromagnets with nonrelativistic spin-momentum coupling, Phys. Rev. X **12**, 011028 (2022).
[10] L. Šmejkal, R. González-Hernández, T. Jungwirth, and J. Sinova, Crystal time-reversal symmetry breaking and spontaneous Hall effect in collinear antiferromagnets, Sci. Adv. **6**, eaaz8809 (2020).
[11] L. Šmejkal, A. H. MacDonald, J. Sinova, S. Nakatsuji, and T. Jungwirth, Anomalous Hall antiferromagnets, Nat. Rev. Mater. **7**, 482 (2022).
[12] R. D. Gonzalez Betancourt, J. Zubáč, R. Gonzalez-Hernandez, K. Geishendorf, Z. Šobáň, G. Springholz, K. Olejník, L. Šmejkal, J. Sinova, T. Jungwirth, S. T. B. Goennenwein, A. Thomas, H. Reichlová, J. Železný, and D. Kriegner, Spontaneous anomalous Hall effect arising from an unconventional compensated magnetic phase in a semiconductor, Phys. Rev. Lett. **130**, 036702 (2023).
[13] L. Han, X. Z. Fu, R. Peng, X. K. Cheng, J. K. Dai, L. Y. Liu, Y. D. Li, Y. C. Zhang, W. X. Zhu, H. Bai, Y. J. Zhou, S. X. Liang, C. Chen, Q. Wang, X. Z. Chen, L. Y. Yang, Y. Zhang, C. Song, J. W. Liu, and F. Pan, Electrical 180° switching of Néel vector in spin-splitting antiferromagnet, Sci. Adv. **10**, eadn0479 (2024).
[14] Z. Y. Zhou, X. K. Cheng, M. L. Hu, R. Y. Chu, H. Bai, L. Han, J. W. Liu, F. Pan, and C. Song, Manipulation of the altermagnetic order in CrSb via crystal symmetry, Nature (London) **638**, 645 (2025).
[15] A. Sakai, S. Minami, T. Koretsune, T. Chen, T. Higo, Y. Wang, T. Nomoto, M. Hirayama, S. Miwa, D. Nishio-Hamane, F. Ishii, R. Arita, and S. Nakatsuji, Iron-based binary ferromagnets for transverse thermoelectric conversion, Nature (London) **581**, 53 (2020).
[16] L. Han, X. Z. Fu, W. Q. He, J. K. Dai, Y. X. Zhu, W. F. Yang, Y. L. Chen, J. C. Zhang, W. X. Zhu, H. Bai, C. Chen, D. Z. Hou, C. H. Wan, X. F. Han, C. Song, J. W. Liu, and F. Pan, Nonvolatile anomalous Nernst effect in Mn_5Si_3 with a collinear Néel vector, Phys. Rev. Appl. **23**, 044066 (2025).
[17] R. A. Leenders, D. Afanasiev, A. V. Kimel, and R. V. Mikhaylovskiy, Canted spin order as a platform for ultrafast conversion of magnons, Nature (London) **630**, 335 (2024).
[18] Z. Zhang, F. Y. Gao, Y.-C. Chien, Z.-J. Liu, J. B. Curtis, E. R. Sung, X. Ma, W. Ren, S. Cao, P. Narang, A. von Hoegen, E. Baldini, and K. A. Nelson, Terahertz-field-driven magnon upconversion in an antiferromagnet, Nat. Phys. **20**, 788 (2024).
[19] J. Krempaský *et al.*, Altermagnetic lifting of Kramers spin degeneracy, Nature (London) **626**, 517 (2024).
[20] Y.-P. Zhu *et al.*, Observation of plaid-like spin splitting in a noncoplanar antiferromagnet, Nature (London) **626**, 523 (2024).
[21] S. Reimers, L. Odenbreit, L. Šmejkal, V. N. Strocov, P. Constantinou, A. B. Hellenes, R. Jaeschke Ubiergo, W. H. Campos, V. K. Bharadwaj, A. Chakraborty, T. Denneulin,

W. Shi, R. E. Dunin-Borkowski, S. Das, M. Kläui, J. Sinova, and M. Jourdan, Direct observation of altermagnetic band splitting in CrSb thin films, Nat. Commun. **15**, 2116 (2024).

[22] Z. X. Feng, X. R. Zhou, L. Šmejkal, L. Wu, Z. W. Zhu, H. X. Guo, R. González-Hernández, X. N. Wang, H. Yan, P. X. Qin, X. Zhang, H. J. Wu, H. Y. Chen, Z. Meng, L. Liu, Z. C. Xia, J. Sinova, T. Jungwirth, and Z. Q. Liu, An anomalous Hall effect in altermagnetic ruthenium dioxide, Natl. Electron. Rev. **5**, 735 (2022).

[23] D.-F. Shao, S.-H. Zhang, G. Gurung, W. Yang, and E. Y. Tsymbal, Nonlinear anomalous Hall effect for Néel vector detection, Phys. Rev. Lett. **124**, 067203 (2020).

[24] A. Gao *et al.*, Quantum metric nonlinear Hall effect in a topological antiferromagnetic heterostructure, Science **381**, 181 (2023).

[25] S.-W. Cheong and F.-T. Huang, Trompe L'oeil ferromagnetism—magnetic point group analysis, npj Quantum Mater. **8**, 73 (2023).

[26] C.-P. Zhang, X.-J. Gao, Y.-M. Xie, H. C. Po, and K. T. Law, Higher-order nonlinear anomalous Hall effects induced by Berry curvature multipoles, Phys. Rev. B **107**, 115142 (2023).

[27] S.-W. Cheong and F.-T. Huang, Altermagnetism with noncollinear spins, npj Quantum Mater. **9**, 13 (2024).

[28] Y. Fang, J. Cano, and S. A. A. Ghorashi, Quantum geometry induced nonlinear transport in altermagnets, Phys. Rev. Lett. **133**, 106701 (2024).

[29] T. Berlijn, P. C. Snijders, O. Delaire, H. D. Zhou, T. A. Maier, H. B. Cao, S. X. Chi, M. Matsuda, Y. Wang, M. R. Koehler, P. R. C. Kent, and H. H. Weitering, Itinerant antiferromagnetism in RuO_2, Phys. Rev. Lett. **118**, 077201 (2017).

[30] Z. H. Zhu, J. Strempfer, R. R. Rao, C. A. Occhialini, J. Pelliciari, Y. Choi, T. Kawaguchi, H. You, J. F. Mitchell, Y. Shao-Horn, and R. Comin, Anomalous antiferromagnetism in metallic RuO_2 determined by resonant x-ray scattering, Phys. Rev. Lett. **122**, 017202 (2019).

[31] Z. H. Lin, D. Chen, W. Lu, X. Liang, S. Feng, K. Yamagami, J. Osiecki, M. Leandersson, B. Thiagarajan, J. Liu, C. Felser, and J. Ma, arXiv:2402.04995.

[32] H. Bai, Y. C. Zhang, Y. J. Zhou, P. Chen, C. H. Wan, L. Han, W. X. Zhu, S. X. Liang, Y. C. Su, X. F. Han, F. Pan, and C. Song, Efficient spin-to-charge conversion via altermagnetic spin splitting effect in antiferromagnet RuO_2, Phys. Rev. Lett. **130**, 216701 (2023).

[33] X. Y. Feng, H. Bai, X. X. Fan, M. H. Guo, Z. Q. Zhang, G. Z. Chai, T. Wang, D. S. Xue, C. Song, and X. L. Fan, Incommensurate spin density wave in antiferromagnetic RuO_2 evinced by abnormal spin splitting torque, Phys. Rev. Lett. **132**, 086701 (2024).

[34] C.-T. Liao, Y.-C. Wang, Y.-C. Tien, S.-Y. Huang, and D. Qu, Separation of inverse altermagnetic spin-splitting effect from inverse spin Hall effect in RuO_2, Phys. Rev. Lett. **133**, 056701 (2024).

[35] Y. B. Fan, Q. Wang, W. Wang, D. Wang, Q. K. Huang, Z. X. Wang, X. Han, Y. X. Chen, L. H. Bai, S. S. Yan, and Y. F. Tian, Robust magnetic-field-free perpendicular magnetization switching by manipulating spin polarization direction in RuO_2/[Pt/Co/Pt] heterojunctions, ACS Nano **18**, 26350 (2024).

[36] Z. Y. Li, Z. Zhang, Y. Z. Chen, S. C. Hu, Y. J. Ji, Y. Yan, J. Du, Y. Li, L. He, X. F. Wang, J. Wu, R. Zhang, Y. B. Xu, and X. Y. Lu, Fully field-free spin-orbit torque switching induced by spin splitting effect in altermagnetic RuO_2, Adv. Mater. **37**, 2416712 (2025).

[37] P. Keßler, L. Garcia-Gassull, A. Suter, T. Prokscha, Z. Salman, D. Khalyavin, P. Manuel, F. Orlandi, I. I. Mazin, R. Valentí, and S. Moser, Absence of magnetic order in RuO_2: insights from μSR spectroscopy and neutron diffraction, npj Spintronics. **2**, 50 (2024).

[38] J. Y. Liu *et al.*, Absence of altermagnetic spin splitting character in rutile oxide RuO_2, Phys. Rev. Lett. **133**, 176401 (2024).

[39] O. Fedchenko *et al.*, Observation of time-reversal symmetry breaking in the band structure of altermagnetic RuO_2, Sci. Adv. **10**, eadj4883 (2024).

[40] S. G. Jeong, I. H. Choi, S. Nair, L. Buiarelli, B. Pourbahari, J. Y. Oh, N. Bassim, A. Seo, W. S. Choi, R. M. Fernandes, T. Birol, L. Zhao, J. S. Lee, and B. Jalan, arXiv:2405.05838.

[41] M. Weber, S. Wust, L. Haag, A. Akashdeep, K. Leckron, C. Schmitt, R. Ramos, T. Kikkawa, E. Saitoh, M. Kläui, L. Šmejkal, J. Sinova, M. Aeschlimann, G. Jakob, B. Stadtmüller, and H. C. Schneider, arXiv:2408.05187.

[42] S. Noh, G.-H. Kim, J. Lee, H. Jung, U. Seo, G. So, J. Lee, S. Lee, M. Park, S. Yang, Y. S. Oh, H. Jin, C. Sohn, and J.-W. Yoo, arXiv:2502.13599.

[43] See Supplemental Material at http://link.aps.org/supplemental/10.1103/rv1n-vr4p for detailed description of sample growth and characterization, effect of driving frequency and roll-offs, third-order Hall response in $RuO_2(110)$ films, size dependence of the TNHE, origin of the TNHE, additional disk device with 16 electrodes, longitudinal resistance of $RuO_2(001)$ in different crystal directions, derivation of angular dependence of the TNHE, second-harmonic transverse response in RuO_2, scaling law, control sample in 30 nm RuO_2, and symmetry analysis of the HNHE in g-wave altermagnets CrSb and MnTe, which includes Refs. [24,28,44–48].

[44] S. Lai, H. Y. Liu, Z. W. Zhang, J. Z. Zhao, X. L. Feng, N. Z. Wang, C. L. Tang, Y. D. Liu, K. S. Novoselov, S. A. Yang, and W.-b. Gao, Third-order nonlinear Hall effect induced by the Berry-connection polarizability tensor, Nat. Nanotechnol. **16**, 869 (2021).

[45] A. Bandyopadhyay, N. B. Joseph, and A. Narayan, Nonlinear Hall effects: Mechanisms and materials, Mater. Today Electron. **8**, 100101 (2024).

[46] Z. Z. Du, C. M. Wang, S. Li, H.-Z. Lu, and X. C. Xie, Disorder-induced nonlinear Hall effect with time-reversal symmetry, Nat. Commun. **10**, 3047 (2019).

[47] Z. H. Gong, Z.-H. Wei, H.-Z. Lu, and X. C. Xie, arXiv:2510.24239.

[48] S.-W. Cheong and F.-T. Huang, Emergent phenomena with broken parity-time symmetry: Odd-order versus even-order effects, Phys. Rev. B **109**, 104413 (2024).

[49] S. Sankar, R. Liu, C.-P. Zhang, Q.-F. Li, C. Chen, X.-J. Gao, J. Zheng, Y.-H. Lin, K. Qian, R.-P. Yu, X. Zhang, Z. Y. Meng, K. T. Law, Q. Shao, and B. Jäck, Experimental evidence for a Berry curvature quadrupole in an antiferromagnet, Phys. Rev. X **14**, 021046 (2024).

[50] K. F. Kang, T. X. Li, E. Sohn, J. Shan, and K. F. Mak, Nonlinear anomalous Hall effect in few-layer WTe2, Nat. Mater. **18**, 324 (2019).

[51] T.-Y. Zhao, A.-Q. Wang, X.-G. Ye, X.-Y. Liu, X. Liao, and Z.-M. Liao, Gate-tunable Berry curvature dipole polarizability in Dirac semimetal Cd3As2, Phys. Rev. Lett. **131**, 186302 (2023).

[52] F. Y. Zhang *et al.*, Crystal-symmetry-paired spin–valley locking in a layered room-temperature metallic altermagnet candidate, Nat. Phys. **21**, 760 (2025).

[53] B. Jiang *et al.*, A metallic room-temperature d-wave altermagnet, Nat. Phys. **21**, 754 (2025).

[54] R. Y. Chu, L. Han, Z. H. Gong, X. Z. Fu, H. Bai, S. X. Liang, C. Chen, S.-W. Cheong, Y. C. Zhang, J. W. Liu, Y. Y. Wang, F. Pan, H. Z. Lu, and C. Song, Data underlying the publication: Third-order nonlinear Hall effect in Altermagnets RuO_2 (4TU, ResearchData.dataset, 2025), 10.4121/f09453b7-5328-4fea-bbfd-3273749d3a40.v1.